energies

*Article*

# Cross-Cutting CFD Support for Efficient Design of a Molten Salt Electric Heater for Flexible Concentrating Solar Power Plants

**Panagiotis Drosatos *, Grigorios Itskos and Nikolaos Nikolopoulos**

Centre for Research and Technology Hellas, Chemical Process and Energy Resources Institute, 6th km. Charilaou-Thermis, GR 57001 Thermi, Greece; itskos@certh.gr (G.I.); n.nikolopoulos@certh.gr (N.N.)
* Correspondence: drosatos@certh.gr; Tel.: +30-211-1069510

**Abstract:** This study focuses on the optimization of an electric heater design for molten salt pre-heating in a supercritical $CO_2$–molten-salt loop. The scope of the investigation is to analyze typical designs of similar components for identifying possible malfunctions and defining proper modifications in the geometry and operating conditions to address such technical issues and optimize the attained thermal efficiency. By performing computational fluid dynamics simulations for reference designs of such components, two particularities pertinent to the temperature distribution are identified as the most likely ones: the development of hot spots and thermal stratification. As a further step, new designs and operating conditions are proposed and their effects on eliminating the hot spots and stratification development phenomena are evaluated. It is shown that the homogeneous distribution of heat flux density across the heating elements is the most favorable option for avoiding the development of hot spots, while the mitigation of thermal stratification is possible through the development of turbulent flow. The proposed design and operating conditions are expected to facilitate the optimization of molten-salt electric heater operation and promote the development of next-generation molten-salt–supercritical-$CO_2$ concentrating solar power plants.

**Keywords:** molten salt; supercritical $CO_2$; CSP plants; electric heater; CFD simulation; design optimization



**Citation:** Drosatos, P.; Itskos, G.; Nikolopoulos, N. Cross-Cutting CFD Support for Efficient Design of a Molten Salt Electric Heater for Flexible Concentrating Solar Power Plants. *Energies* **2023**, *16*, 6403. https://doi.org/10.3390/en16176403

Academic Editor: Sandro Nizetic

Received: 20 June 2023
Revised: 2 August 2023
Accepted: 4 August 2023
Published: 4 September 2023



## 1. Introduction

Concentrated solar power (CSP) is a well-established technology for renewable energy (RE) generation at scale [1,2]. In CSP, solar collectors (the so-called heliostats) are used for providing concentrated, high-temperature heat to a heat transfer fluid (HTF) in the power tower; such thermal energy is then directly stored in a tank or converted to mechanical work in a turbine or transferred to a working medium for running a thermodynamic cycle [3,4]. Currently, the Rankine cycle is the most widely exploited thermodynamic cycle in CSP plants [5]. However, supercritical $CO_2$ ($sCO_2$) Brayton cycles have recently been proposed [6] for replacing such conventional water/steam and organic Rankine cycles, and are increasingly gaining momentum for implementation in next-generation CSP plants, due to their strong potential for yielding further cost reductions and enhanced efficiencies. Indeed, the implementation of $sCO_2$ Brayton cycles in CSP can facilitate higher turbine inlet temperatures and, since $CO_2$ is, in general, less corrosive than water/steam, under certain circumstances may also pose fewer material selection challenges [7]. Furthermore, system operation beyond the critical point of the working fluid can provide the deployment of smaller turbomachinery and heat exchangers, compared to the respective component sizes in systems driven by conventional water/steam Rankine power cycles. In addition, the relatively high efficiency of $sCO_2$ Brayton cycles in the case of dry cooling renders them ideal for implementation in a severe drought area, that is, a typical CSP infrastructure environment [6]. Notably, it was shown recently [8] that even the simplest form of an $sCO_2$ Brayton cycle has the potential to achieve the same efficiency as an equivalent size (in MW), superheated steam Rankine cycle operating at similar conditions, sparking further interest in this technology.

In 2020, there were over 25 GWs of installed CSP capacity worldwide [9]. Should the reported growth trends maintain their current pace and reach their prospective potential, CSP is expected to be able to cover up to 25% of the world's energy needs by 2050 [10], thereby critically facilitating the large-scale penetration of renewable solar energy into the electricity grid. One of the main competitive attributes of CSP plants driving such growth is that heat from sunlight can be readily transferred to, and retained in, thermal energy storage (TES) media, such as molten salts, to allow for rapidly dispatchable and/or continuous power [11]. Indeed, through the integration of a molten-salt-based TES system, CSP can provide: (i) a high capacity value, (ii) the ability to shift energy production to periods of high value, and (iii) a remarkable source of low-carbon grid flexibility [12], thereby addressing the inherent intermittency and uncertainty challenges associated with the grid-scale penetration of renewable energy [13]. Molten nitrate salts (e.g., 60 wt% sodium nitrate and 0 wt% potassium nitrate, known as "solar salt") have commonly been used for heat transfer and TES in CSP installations [14–16], with earth-abundant molten chlorides having been recently proposed for this scope as well [17,18].

In the case of molten-salt heat transfer/TES utilization, the indirect integration scheme is mandatory, even if such a scheme may entail energy losses and a pressure drop due to the use of intermediate heat exchangers [19,20]. In light of facilitating such indirect molten-salt–s$CO_2$ Brayton cycle integration, the use of an electric heater for heating-up the salt is essential (note that the implementation of such a heater can be cost-effective as well, as it can be powered by excess RE from the grid). Indeed, the development of robust, flexible molten-salt electric heaters is widely recognized as a crucial priority, both for enabling a more efficient CSP operation and for further facilitating the integration of CSP technology with other RE generation technologies, since the employment of such electric heaters is essential for reducing PV and/or wind turbine output fluctuations and energy curtailment.

As the electric heater can be a critical component in the operation of an integrated CSP/TES/RES industrial scheme, considerable research has been conducted over the last several years across a wide range of topics pertinent to the use of such electric heaters or molten salts in a CSP environment. From an assessment standpoint, such research has focused either on techno-economics and experiments, evaluating a CSP system in a stand-alone mode or in conjunction with other RES sub-systems [21–23] , or on the salt and containment material properties and the associated corrosion mechanisms for selection of suitable materials for use in integrated molten-salt-tank–electric-heater systems [24–26]. It is noted that in the techno-economic and experimental studies, the electric heater was considered only a part of a bigger inter-connected system, while in the respective material-focused reports, electric heater design considerations were not taken specifically into account. Recently, Mahdi et al. [27] performed a computational fluid dynamics (CFD) investigation on an optimized design of an electric heater with the proposed configuration being very similar to the design indicated as ideal for integration in CSP plants in our current paper. However, Mahdi et al.'s case presents a significantly lower capacity (600 kW) than the MW-scale capacity needed in next-generation CSP plants. It is, therefore, a current necessity that optimal design and construction configurations for such molten salt heaters be obtained, with the scope of improving their overall thermal performance and efficiency. To accomplish this, we need to establish optimized trade-offs between reaching the full heat transfer potential of molten salts and avoiding coming too close to their degradation temperature.

In this vein, we employ here CFD simulations using the ANSYS Fluent® software (https://www.ansys.com/products/fluids/ansys-fluent accessed on 3 August 2023) package for modeling the behavior of a 7 $MW_e$ electric heater (designed by SEICO GmbH, Langenhagen, Germany) and obtaining detailed insights on the complicated flow, thermal transfer, turbulence, and radiation phenomena that occur within the domain of such a heater. The novel aspect of this study lies primarily in the synergistic interaction between a CFD tool and a proprietary design program developed by SEICO GmbH. This amalgamation serves the purpose of identifying potential practical challenges associated with the operation of a molten-salt electric heater component. Moreover, such interaction facilitates the precise delineation of necessary modifications in the geometry of a heater.

Indeed, based on the simulation results of the initial design, it became evident that certain factors related to the operating conditions and component design could potentially increase the risk of thermal stratification and the formation of hot spots. To address this concern, an optimized design is proposed here. This optimized design incorporates a horizontal configuration with perpendicular baffles arranged at a small pitch and features low cross-sectional baffle windows. These design modifications significantly enhance the turbulence intensity within the system. By increasing the turbulence, the risk of thermal stratification in the electric heater is mitigated, effectively reducing the likelihood of hot spots' formation.

Overall, this work paves the way for targeted redesign efforts of such components that leverage CFD analysis, enabling the development of more effective and efficient electric heaters for molten salt application in next-generation CSP plants.

## 2. Initial Heater Design

### *2.1. Process Conditions*

The electric heater under consideration has been sized as per the parameters of a molten salt mixture that consists of sodium nitrate (60%) and potassium nitrate (40%). According to data provided by SEICO GmbH, the physical properties of the fluid over the operation range of 380 °C to 580 °C can be estimated from Equations (1)–(4), where T is the temperature in Kelvin, except for the dynamic viscosity where T is the temperature in °C:

$$\text{Specific Heat Capacity} = -1 \times 10^{-10}\ \mathrm{T}^3 + 2 \times 10^{-7}\ \mathrm{T}^2 + 5 \times 10^{-6}\ \mathrm{T} + 1.4387 \tag{1}$$

$$\text{Density} = -1 \times 10^{-7}\ \mathrm{T}^3 + 2 \times 10^{-4}\ \mathrm{T}^2 - 0.7875\ \mathrm{T} + 2299.4 \tag{2}$$

$$\text{Dynamic Viscosity} = -1.473302 \times 10^{-10}\ \mathrm{T}^3 + 2.279989 \times 10^{-7}\ \mathrm{T}^2 - 1.199514 \times 10^{-4}\ \mathrm{T} + 0.02270616 \tag{3}$$

$$\text{Conductivity} = -1 \times 10^{-11}\ \mathrm{T}^3 + 3 \times 10^{-8}\ \mathrm{T}^2 + 2 \times 10^{-4}\ \mathrm{T} + 0.3922 \tag{4}$$

These equations yield the values shown in Table 1 for the physical properties of this molten salt mixture over the temperature range pertinent to the operation of the molten salt heater here.

**Table 1.** Molten salt properties against temperature.

| Temperature | Temperature | Specific Heat Capacity | Density | Dynamic Viscosity | Conductivity |
|---|---|---|---|---|---|
| °C | K | kJ/kg/K | kg/m$^3$ | Pa s | W/m/K |
| 380 | 653.15 | 1.499 | 1842.5 | 0.0019634 | 0.533 |
| 400 | 673.25 | 1.502 | 1829.4 | 0.0017763 | 0.537 |
| 420 | 693.15 | 1.505 | 1816.3 | 0.0016302 | 0.542 |
| 440 | 713.15 | 1.508 | 1803.2 | 0.001518 | 0.546 |
| 460 | 733.15 | 1.510 | 1790.1 | 0.0014326 | 0.551 |
| 480 | 753.15 | 1.513 | 1777.0 | 0.0013669 | 0.556 |
| 500 | 773.15 | 1.516 | 1763.9 | 0.0013139 | 0.560 |
| 520 | 793.15 | 1.519 | 1750.7 | 0.0012665 | 0.565 |

**Table 1.** *Cont.*

| Temperature | Temperature | Specific Heat Capacity | Density | Dynamic Viscosity | Conductivity |
|---|---|---|---|---|---|
| °C | K | kJ/kg/K | kg/m$^3$ | Pa s | W/m/K |
| 540 | 813.15 | 1.521 | 1737.5 | 0.0012177 | 0.569 |
| 560 | 833.15 | 1.524 | 1724.3 | 0.0011603 | 0.574 |
| 580 | 853.15 | 1.526 | 1711.0 | 0.0010873 | 0.578 |

From the various factors incorporated in Equations (1)–(4), the most critical ones for determining the initial sizing of the heater are the specific heat capacity and the density of the salt. The values selected here for the subsequent sizing calculations are 1.513 kJ/kg/K and 1777 kg/m$^3$, which are the respective median values for such salt properties. The mass flow rate was defined at 22.22 kg/s. The inlet temperature was selected to be 380 °C for ensuring a sufficient margin between the inlet temperature and the highest melting point of the salt mixture, i.e., 322 °C. The outlet temperature was computed at 580 °C for validation purposes of the CFD tool, which is marginally below the point where degradation products start to form (>600 °C). The operating pressure was selected to be 3 bar to match the operating pressure of the molten salt system. Note here that in the original electric heater design configuration, the intended pressure drop was 0.3 bar; nonetheless, once it was established that a substantially more constricted internal baffle arrangement was required, the allowable pressure drop was increased to a maximum 1 bar.

### *2.2. Initial Heater Sizing*

SEICO GmbH, part of the Exheat Group, utilizes a proprietary program from their parent company Exheat Ltd. (Watton, UK) for sizing electric heaters. Given the fluid properties, system process parameters, and the electrical system data, the software calculates the necessary power the heater should provide (7 MW$_e$), initial geometric features (baffle pitch = 260 mm), as well as a first definition of the number of necessary heating elements (~550), and their geometric details (diameter = 12.5 mm, tube pitch = 24 mm). It is important to note that, as this is an initial design being developed in subsequent tasks, the heater includes some design margins. Based on the initial sizing and the agreed process conditions (pressure drop, temperature levels, working medium mass flow rate), it was possible to generate the computer-aided design (CAD) model for use in CFD simulations. Figure 1a shows the CAD drawing of such a model, and (b) the initial geometric model that after proper modifications is used in the CFD analyses.

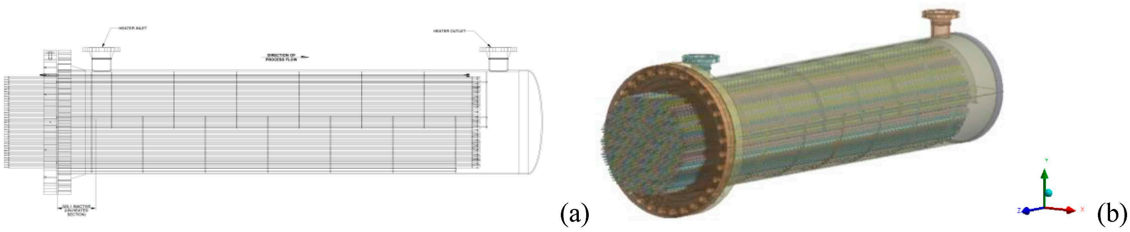


**Figure 1.** Preliminary design for the molten salt electric heater: (**a**) CAD drawing, (**b**) geometric model for the CFD simulations.

The scope of CFD here is to enable the electric heater designer to fine tune the internal design and the heat transfer distribution by possibly modifying: (a) the internals, (b) the distribution of elements, (c) the heat flux density upon the element surface in different sections of the heater, (d) the location of the element sensors, and (e) the control methodology. The overall intention is to provide a far smoother increase in the fluid temperature as it passes through the electric heater whilst ensuring that the heating elements do not exceed the degradation temperature limits previously highlighted.

### 2.3. CFD Simulation of the Initial Heater Design

CFD simulations of the electric heater were conducted for three different design configurations, namely the Benchmark, the Configuration 1, and Configuration 2 scenarios. The principal difference between these three cases lies on the assumption made about the direction of the gravity vector, resembling a different structural orientation in each given case. Figure 2 shows, comprehensively, schematics of the three configurations taken into account here, including the gravity vector direction in each case. More specifically, Configuration 1 foresees the vertical orientation of the structure with inlet nozzle above the outlet nozzle, so that the fluid descends through the heater. The termination box is at the top of the heater, which is typical for vertical electric heaters of the type considered here. Configuration 2 foresees the horizontal orientation of the structure, purely rotated 90 degrees around its axis so that the baffles sit on either side of the vertical plane and the nozzles are horizontal.

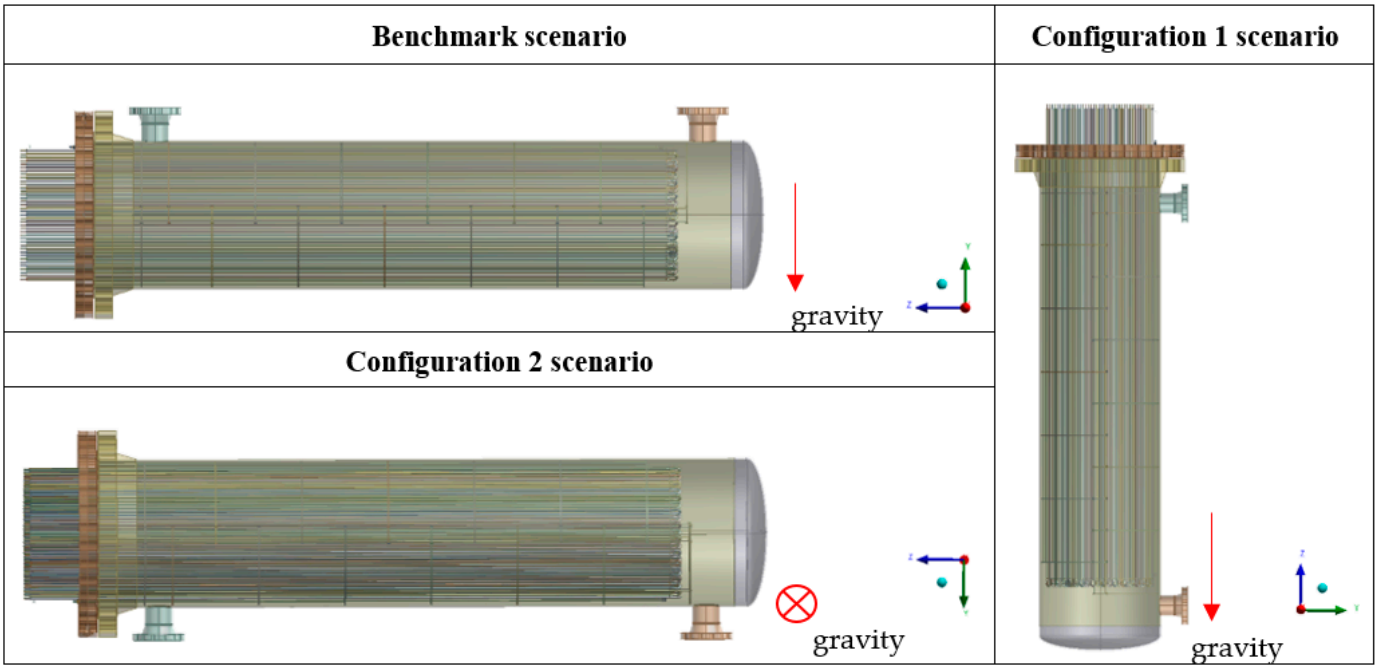


**Figure 2.** Geometric models of the electric heater pertinent to the three different configurations tested in the numerical simulations.

Regarding the mathematical models, the turbulence was simulated using the k-ε turbulence model along with standard wall functions, while the radiation was simulated with the P1 model. As concerns the implemented boundary conditions, the inlet mass flow rate, inlet pressure, and the corresponding temperature were all defined by the designer of the component. However, in order to simplify the problem, the geometric model corresponded to a half of the real geometry with fully symmetrical conditions having been implemented. Therefore, the applied mass flow rate was correspondingly half the design value (11.11 kg/s). The shell surfaces (outer bounds of the computational domain) were 9.5 mm thick and composed of ASTM A312 347 material. The elements of the electric heater were 0.7 mm thick and composed of Incoloy Alloy 825. In both these groups of surfaces, the shell conduction model was applied. According to this model, the heat transfer in electric elements and shell walls is considered in all three directions. Furthermore, the heat duty of the electric heater elements was taken as equal to 3.5 $MW_{th}$ (half of the total 7 $MW_{th}$). This heat duty is translated to 48,229 $W/m^2$ wall heat flux density (total exterior area of heating elements ~72.6 $m^2$). In addition, thermal convection boundary conditions were implemented upon the shell surfaces for taking into account the heat losses of the component to ambience. For defining such boundary conditions, the free stream temperature was taken as ~ 27 °C along with a convective heat transfer coefficient equal to 10 W/m$^2$/K. Finally, the baffle surfaces were considered adiabatic.

The solution was performed by assuming steady-state conditions. To assess the convergence of the solution, we employed a set of specific criteria. For the initial design case, these criteria were set at $1 \times 10^{-3}$ for continuity, velocity, and the k-ε turbulence equations, while $1 \times 10^{-6}$ was used for the energy and P1 radiation model. However, convergence was judged not only by examining scaled residual levels, but also by monitoring the working medium average temperature (at the outlet surface) and the velocity magnitude of the flow (at specific points of the domain). For the initial design solution, we employed two AMD EPYC 7302P servers, each equipped with 16 cores and 64 GB of RAM. Achieving convergence for this solution required nearly a full day of computation time.

Developed Temperature Field

The working medium temperature distribution as provided by the CFD simulations at the characteristic middle plane (x = 0) of the component for each of the three examined scenarios is shown in Figure 3.

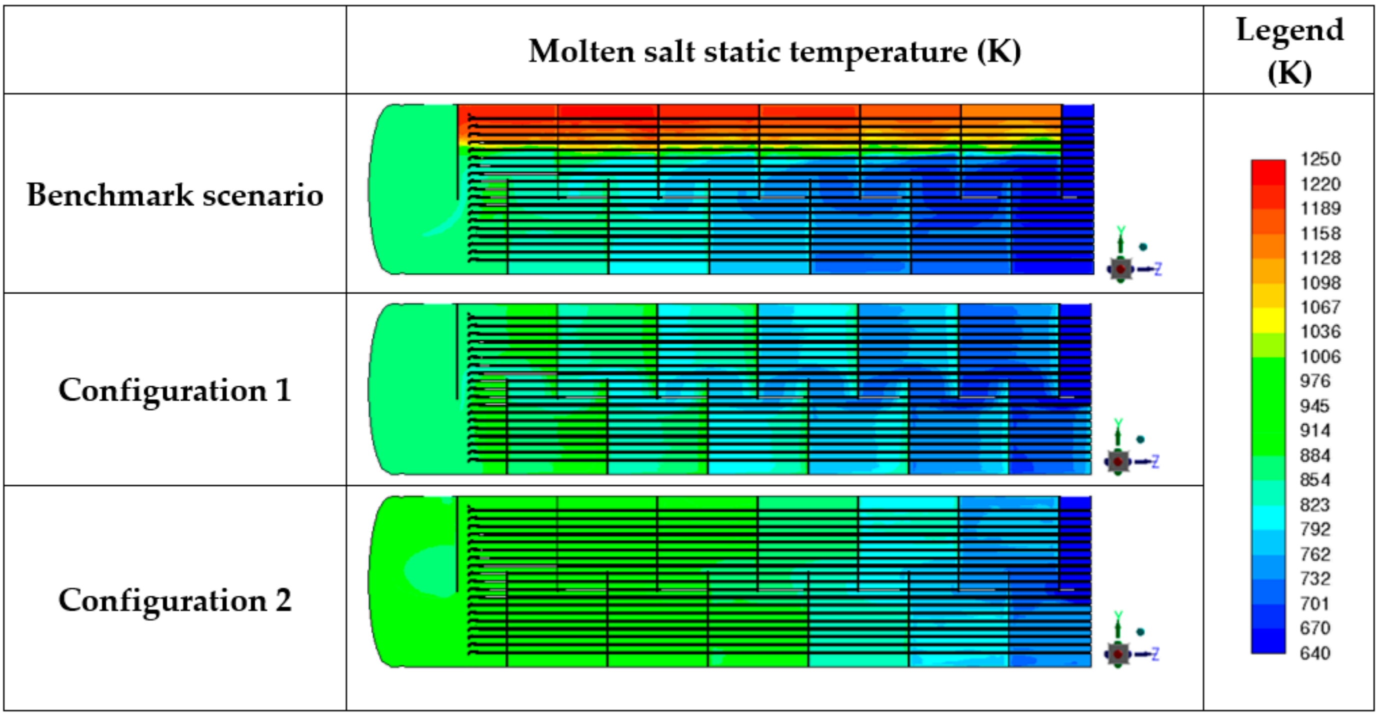


**Figure 3.** Molten salt temperature distribution (K) in Benchmark, Configuration 1, and Configuration 2 scenarios.

Based on the derived results, in the Benchmark scenario, the highest temperature values were detected at the upper levels of the heater between all baffles. The mechanism behind this temperature field is buoyancy. The development of stratified flow layers depresses the mass flow rate of the molten salt at the upper levels of the heater (after the first baffle), thereby creating the observed hot spots.

As concerns Configuration 1, the following observations were made: (a) there is a snaking path of cooler fluid running down the central line of the heater, (b) there are regions of relatively cooler fluid upstream of each baffle, and (c) there are thin layers of relatively hotter fluid downstream of each baffle. There are two possible explanations for the calculated hot stagnant zones downstream of the baffles: either (a) there are stationary vortexes, which may create stagnation points, thus locally exposing the fluid to intense heat up, and/or (b) under the effect of buoyancy, hotter fluid is concentrated on the underside of each baffle and cooler fluid is concentrated on the top side.

As concerns Configuration 2, the developed temperature field in the latter two thirds of the heater appeared to be more homogeneous, while the average temperature of each stage also appeared to be higher than the equivalent value of the same stage in the case of Configuration 1. What is more, a region of relatively cooler fluid was identified after the last baffle, in a shape that suggests the formation of a recirculation zone. This vortex draws cooler fluid from the lower layers of the heater (+x areas), thus decreasing the developed average temperature values.

Furthermore, Configuration 2 case presented the highest temperature values near the centerline of the electric heater (not obvious in Figure 3) due to implementation of the symmetric boundary conditions, as only half of the geometry was simulated. In actual conditions, these high-temperature regions are expected to manifest at the uppermost sections of the electric heater (−x), in the opposite direction of the gravity vector, influenced by buoyancy. Thus, this simulation serves as an initial investigation case for assessing the probability of thermal stratification. To accurately predict the temperature field for this specific configuration, a complete simulation of the entire heater is required.

In order to ensure the validity of the derived results, a grid independence study was also performed. By applying the mesh refinement technique provided by ANSYS Fluent®, a denser grid comprising 37,267,940 elements was developed (the initial grid consisted of 5,560,297 elements). The results derived by this sophisticated grid reaffirmed the development of thermal stratification, showing that this flow structure was a malfunction arising from the initial design and the selected operating conditions (rather than a consequence of the grid quality). Except for the grid independence study, efforts were also made to ensure the validity of the results based on theoretical principles, because experimental data were not available. The initial design conditions induce laminar flow, which can cause the formation of stratified layers when gravitational and viscous forces outweigh inertial forces. Furthermore, the results are in accordance with the conclusions derived by [27], which highlight that optimized values of geometric features (clearances, number of baffles, etc.) of a similar electric heater are capable of promoting turbulent conditions and eliminating the risk of the formation of dead zones and hot spots. Since, in our case, the flow is laminar and the design is not optimized, it is very likely that the mathematical model provides a reasonable representation of the actual operating conditions. To further validate such findings, additional tests were conducted by varying the inlet velocity or, equivalently, the mass flow rate of the working medium. In cases where turbulent conditions were present, the inertial forces successfully disrupted the stratified layers, resulting in a homogeneous temperature distribution, which is consistent with the underlying theory.

Based on the obtained results, it can be observed that Benchmark and Configuration 2 scenarios exhibit intense thermal stratification. To minimize the risk for thermal stratification, it is crucial to consider a geometric configuration with vertical orientation. This configuration involves aligning the length of the component parallel to the gravity vector, such as in the case of Configuration 1. However, the length of the electric heater is too extensive to be accommodated within a structure if it needs to be vertically oriented. Consequently, it is imperative to appropriately modify the initial design or the implemented conditions to ensure flow turbulence and eliminate any stratified layers. Overall, it can be concluded that the phenomenon of thermal stratification is highly dependent on the design of the heater or the operating conditions that may result in inertial forces not strong enough over gravity and viscous forces. In that case, the modification of geometry or/and operating conditions is essential for achieving efficient heat transfer and preventing thermal stratification.

## 3. Revised Design of the Electric Heater for Eliminating Thermal Stratification

Based on the modeling outcomes discussed above, a new electric heater design featuring horizontal orientation was developed, where significant turbulence of the flow can be achieved, and the formation of stratified flow layers can be avoided. Since it was necessary to maintain a turbulent flow regime, it was required to implement a working fluid flow with higher than initial momentum (Re > 10,000 for the whole component). This, in general, can be achieved by restricting the cross-sectional area. In this light, two possible solutions were determined: (a) to place multiple smaller-diameter heaters in a stacked arrangement, and (b) to place a baffle arrangement of a perpendicular type with smaller pitch and lower cross-sectional baffle windows in the existing heater that contorts the flow both up and down and side to side by utilizing a central longitudinal plate. Between these two alternatives, the latter option was adopted, as this would be the lowest cost option in terms of fabrication and materials. Note that the longitudinal plate only blocks the top 60% of the diameter of the heater. The perpendicular baffles have alternating top baffle windows. Thus, the path of the fluid is as follows:

(1) Travels up between two baffles on the right-hand side;
(2) Through the baffle window;
(3) Travels down between two baffles on the right-hand side;
(4) Under the longitudinal plate;
(5) Travels up between two baffles on the left-hand side;
(6) Through the baffle window;
(7) Travels down between two baffles on the left-hand side;
(8) Under the longitudinal plate;
(9) Repeat until the end of the electric heater.

The final design of the electric heater takes into consideration two more parameters: (a) the pressure drop within the heater, and (b) the existence of leakages around the baffles. Due to fabrication tolerances, there will always be a gap between the baffles and the shell, through which a small portion of the fluid may pass, thereby deviating from its optimal path. Within a conventional electric heater, such as the one depicted in the Benchmark configuration (with just a dozen baffles), such leakages would likely not be significant. However, within a novel configuration with a longitudinal plate and tightly pitched baffles, there would be significantly more leakage paths, so it is important that these are taken into consideration in the CFD simulations of the final electric heater design.

The final design of the electric heater is shown in Figure 4.

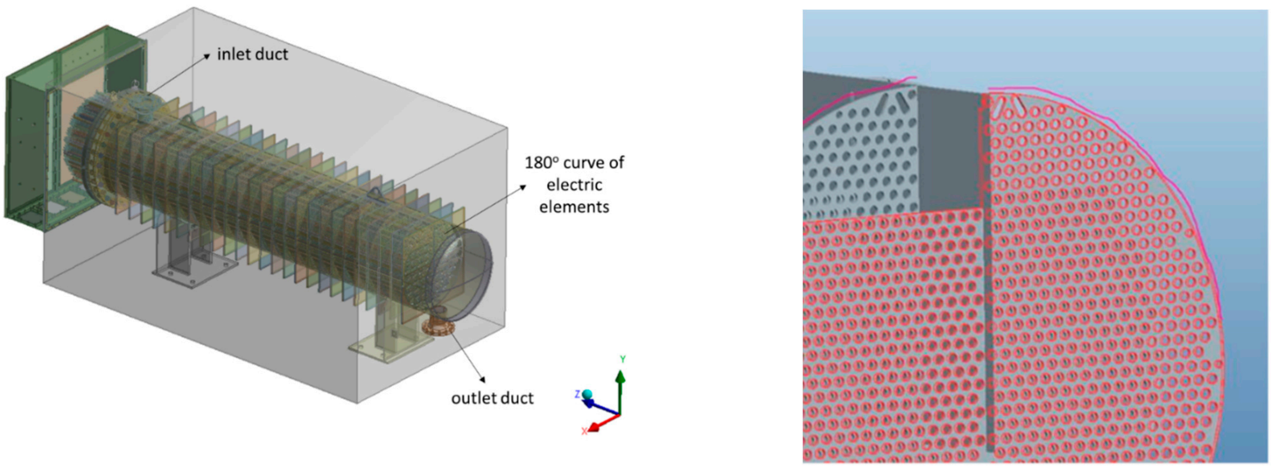


**Figure 4.** Final design of the electric heater geometry developed by SEICO GmbH.

### *3.1. CFD Simulation of the Final Heater Design*

#### 3.1.1. Geometry, Developed Numerical Grid, and Mathematical Models

As a first step, suitable actions were performed in order to formulate the domain for the conduction of the CFD simulations. This domain represents the volume, where the molten salt flows. The result is presented in Figure 5.

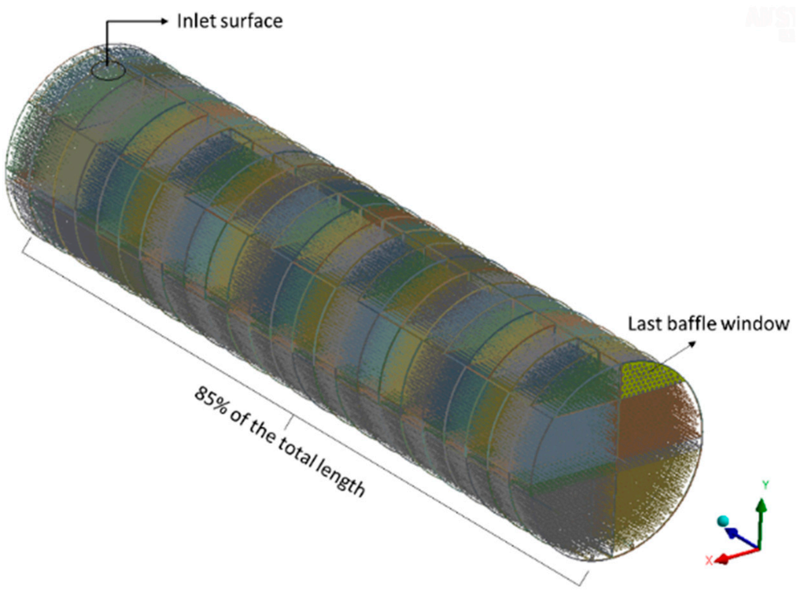


**Figure 5.** Geometric model developed based on the electric heater final design.

As can be seen upon observing Figure 5, the geometric model developed for the CFD simulations did not consider all the length of the heater. More specifically, the final part of the electric heater that includes the outlet duct and the 180° curve of the electric heater elements was omitted. This simplification was performed in order to develop a numerical grid that combines an acceptable total number of elements and high quality. More specifically, the complicated geometric features of the electric heater curves would have demanded an extremely large number of numerical elements for being sufficiently discretized, thereby substantially increasing the demand for computational resources and computation time. Instead, the remaining part of the electric heater, representing almost 85% of its total length, was approximated in high detail, taking into account all the geometric features (i.e., gaps between baffles and shell, all heating elements, etc.) to increase the accuracy of the derived results and approximate as closely as possible the real operating conditions of the heater. Moreover, the length considered in this final design simulation was evaluated as sufficient to accurately approximate the total pressure drop, since all baffle configurations, except for the last one, have been taken into account. Furthermore, even if the curved formations of the heating elements result in additional pressure losses, these are expected to be a small fraction compared to the total pressure losses resulted by all the geometric characteristics of the component. In addition, the part downstream of the curved features of the electric heater elements is not expected to significantly contribute to the overall pressure losses of the working medium, since it is apparently a domain that does not impose obstacles to the flow. Therefore, the outcomes for the developed flow can be considered very close to the real case. Finally, the geometric model of the electric heater has been divided into numerous sub-volumes to enable the use of the sweep methodology for the development of the numerical grid. Indeed, this technique enables the discretization of the domain with the highest possible quality and the lowest number of total elements. The sweep methodology was applied in all the regions of the component, except for the areas adjacent to the circular formation of the inlet surface.

In order to better handle the geometry during the meshing procedure, this was divided into two parts; i.e., Part A and Part B (see Figure 6). Part A refers to the inlet surface and the adjacent volumes, whereas part B refers to the rest of the modeled domain. As previously mentioned, Part A was characterized by some volumes that could not be discretized with the sweep methodology, thus requiring the utilization of a hybrid mesh technique. Furthermore, since Part A is basically the inlet domain of the electric heater component, this had to be discretized in high detail in order to better approximate the complicated phenomena occurred at the initial stages of the molten salt flow owing to the inlet stream (recirculation zones) and avoid convergence issues or error diffusion.

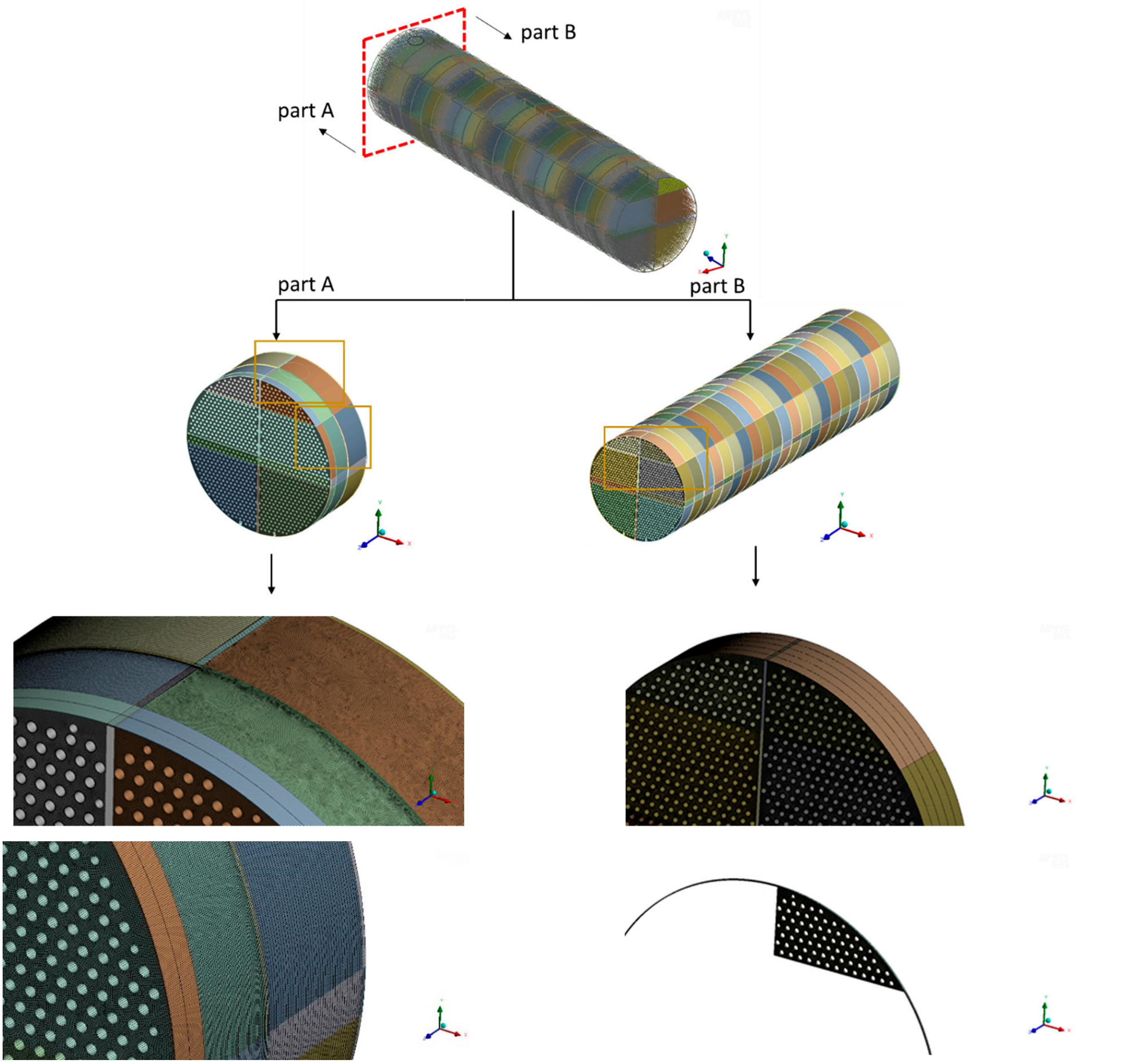


**Figure 6.** Numerical grid developed by CERTH based on the final SEICO GmbH electric heater configuration.

In total, 25,888,923 elements were used to approximate the whole geometry under investigation. Approximately 35% of them (i.e., 9,016,561 elements), were included in Part A, and the remaining 65% (i.e., 16,872,362 elements) were included in Part B. The overall distribution of the elements based on their type was as follows: 0.1% tetrahedrons, 98.12% hexahedrons, 1.6% wedges, and 0.18% pyramids. The fact that the vast majority of the elements were hexahedrons is important for ensuring a smooth solution procedure and no convergence issues. The distribution of the elements based on their type for each of the two domain parts was as follows: 0.30% tetrahedrons, 97.34% hexahedrons, 1.88% wedges, and 0.48% pyramids for Part A, while there were 98.54% hexahedrons and 1.46% wedges for Part B. It is noteworthy that Part B did not include any tetrahedron or pyramid. Figure 6 presents characteristic views of the developed numerical grid in both sub-domains.

Given the total number of cell elements and the average cell element size for the near-wall region (adjacent to electric heater elements) that is equal to 2.5 mm, it is obvious that a very dense numerical grid was constructed in order to perform high-resolution numerical simulations. The utilization of a highly refined grid ensures accurate and validated results concerning the flow and heat transfer conditions. Regarding the attained quality, this can be characterized as sufficiently high, even if there were some elements with a skewness factor greater than the upper acceptable limit (0.94). More specifically, 33% of tetrahedrons (i.e., 8967 elements), 0.05% of hexahedrons (i.e., 4434 elements), 1.6% of wedges (i.e., 2721 elements), and 1.93% of pyramids (i.e., 828 elements) in the Part A domain presented a skewness factor greater than 0.94. Almost 1.7% of the wedges (i.e., 4200 elements) presented the same skewness factor greater than 0.94 in the Part B domain. Overall, only 0.08% of the elements were characterized by low quality and these were merely located in areas close to the outer bounds of the computational domain, including the gaps between the baffles and shell walls. Therefore, the spatial distribution of these low-quality elements in areas of low mass flow-rate and their small percentage compared to the total number of elements ensure the low possibility for convergence issues and error diffusion. If, however, any error diffusion happens, it will be located in areas with low significance and not in the main flow domain. Finally, two layers were developed close to the electric heater elements (see Figure 7). Since the smooth transition option was enabled for the construction of such elements (maximum layers = 2, growth rate = 1.2), and given the average cell element size as discussed above, the first layer thickness is ~586 μm. The grid development technique ensured y+ values lower than 5 and turbulence Reynolds numbers lower than 200 to a significant extent of the near-wall region, even if only two layers were implemented. However, the high discretization of the areas close to the electric heater elements and the very low y+ values imposed the necessity of implementing the SST k-omega model, instead of the k-ε model with standard wall functions. Furthermore, due to the high complexity of the geometry, it was considered that the accuracy of the P1 radiation model may be affected. Instead, the DO radiation model was used.

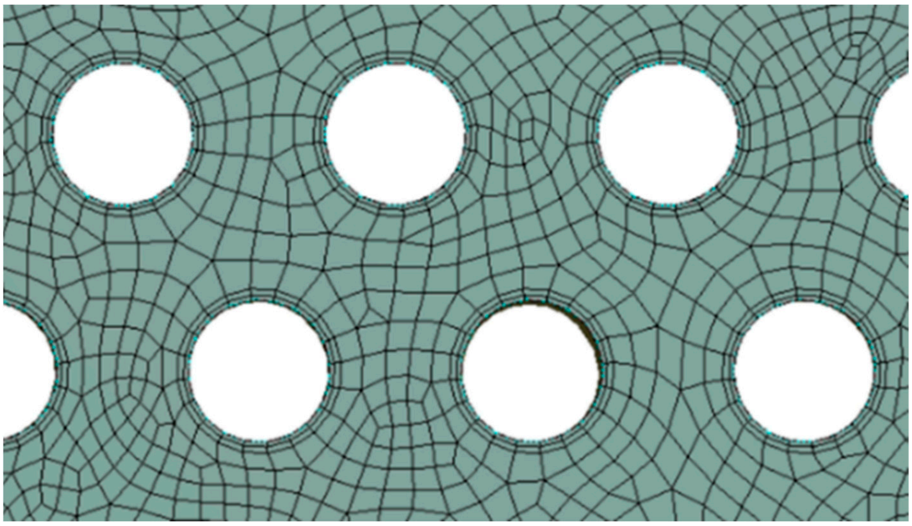

**Figure 7.** Grid development around the electric heater elements.

Tables 2 and 3 present the models and boundary conditions selected for the numerical simulations regarding the final design of the electric heater component. It must be underlined that the shell conduction model was applied only for the shell wall surfaces. In addition, these surfaces were characterized by a thermal convection boundary condition. Furthermore, the surfaces of the baffle formations have been considered adiabatic. Regarding the heat flux density of the electric heater elements, two different scenarios have been considered. The first, subcase 1, assumed constant value throughout the element length, i.e., 45,836 W/$m^2$, considering that the total heat transfer towards the working medium is equal to 7 $MW_{th}$ and the area of the elements providing heat ~152.7 $m^2$, while the second, subcase 2, assumed a specific spatial distribution. More specifically, it was supposed that 80% of the total duty (5.6 $MW_{th}$) is delivered in the first 60% of the length of the heater (~an area of 91.6 $m^2$ of the elements provides heat); thus, resulting in a heat flux density equal to 61,115 W/$m^2$. Meanwhile, the remaining 20% of the heat duty (1.4 $MW_{th}$) is implemented in the remaining 40% of the element's length; thus, resulting in a heat flux density equal to 22,918 W/$m^2$ (see Figure 8). This specific configuration was implemented through an appropriately developed user-defined function. In addition, it was considered that the first part of the electric heater elements, just below the inlet surface, did not provide any heat. Furthermore, the final design guarantees turbulent flow conditions, resulting in significantly enhanced heat transfer towards the working medium (molten salt) through convection mechanisms, surpassing the heat transfer along the electric heater elements through conduction. As a result, the implementation of the shell conduction model was no longer required, and the consideration of thickness has been omitted. Finally, since the whole geometry of the electric heater was considered, the mass flow rate of the working medium in the CFD simulations was equal to the reference value, i.e., 22.22 kg/s, and no symmetric conditions were considered.

**Table 2.** Implemented models in the CFD simulations for the final design of the electric heater.

| | **Final Design Scenario** |
|---|---|
| Simulations | 3D simulations<br>Steady-state conditions<br>Single phase |
| Turbulence model | SST k-omega |
| Radiation | DO radiation model |
| Evaluation of gradients | Green–Gauss Node-Based |
| Pressure interpolation schemes | Standard |
| Gravity vector | -y |

**Table 3.** Implemented boundary conditions in the CFD simulations for the final design of the electric heater.

| | **Final Design Scenario** |
|---|---|
| Inlet | Mass flow rate: 22.22 kg/s<br>Pressure: 3 bar<br>Temperature: 653.15 K (380 °C) |
| Symmetric conditions | NO |
| Elements | Material: Incoloy Alloy 825<br>Properties: k = 11.1 W/m/K<br>Constant heat flux density (45,836 W/$m^2$) or spatially distributed |
| Shell Walls | Thickness: 9.5 mm<br>Material: ASTM A312 347<br>Properties: k = 14.88–21.5 W/m/K<br>Thermal convection (h = 10 W/$m^2$/K and external T = 300 K)<br>Shell conduction model |
| Baffle Walls | Adiabatic |

The solution was performed by assuming steady-state conditions. To assess the convergence of the solution, we employed a set of specific criteria. For the final design case, these criteria were t $1 \times 10^{-3}$ for continuity, velocity, and the k-omega turbulence equations, while $1 \times 10^{-6}$ was used for the DO radiation model and $1 \times 10^{-7}$ for the energy equation. However, convergence was assessed not only by examining scaled residual levels, but also by monitoring the working medium average temperature at the outlet surface and the velocity magnitude of the flow at specific points of the domain. For the final design solution, we employed four AMD EPYC 7302P servers, each equipped with 16 cores and 64 GB of RAM. The solution process for the final design took a couple of days to reach convergence.

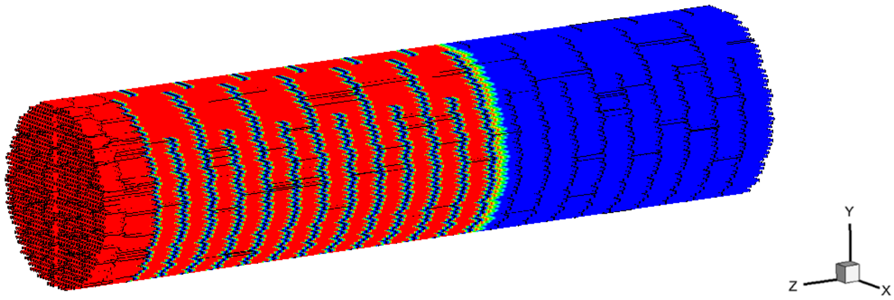


**Figure 8.** Spatial distribution of the heat flux density of the electric heater elements (red: 61,115 W/m$^2$ and blue: 22,918 W/m$^2$).

Finally, in order to ensure the validity of the derived results, a grid independence study was conducted. More specifically, the numerical grid underwent refinement within a cylindrical domain (specifically along the centerline of the structure), confined within a radius of 0.1 m and extending between z = −3 m and z = −0.5 m (note that the overall length of the component spans from z = −3.813 m to z = −0.181 m). Through the mesh refinement feature offered by ANSYS Fluent®, the grid was extensively refined, resulting in the formulation of a denser grid comprising approximately 31.4 million elements, as opposed to the initial grid size of about 26 million elements. To compare the results between the two cases, i.e., the final design with both the initial and refined numerical grids, we employed two lines, each consisting of thirty-four points. The first was positioned within the refined domain, while the second was placed at the interface between the initial and the sophisticated (refined) region. These lines allowed us to derive the velocity components and temperature distribution along the electric heater's length. The comparison between these two numerical grids indicated a satisfactory agreement. In fact, the highest percentage relative difference for the critical parameter of the flow temperature was below 2%.

### 3.1.2. CFD Results on Temperature Field

Figures 9–11 present the spatial distribution of the molten salt static temperature at characteristic transversal surfaces for both subcases. Symbol (a) is used for the case with homogeneous heat flux density, while symbol (b) is used for the case with spatially distributed heat flux density. The first graph, Figure 9, presents the spatial distribution of the working medium temperature for both cases at specific +x planes that are 0.4 m, 0.336 m, and 0.224 m away from the electric heater centerline (x = 0). Figure 10 shows the same spatial distribution at the +x, −x planes that are very close to the electric heater centerline (just 0.112 m away), and Figure 11 at the respective −x planes of Figure 9. Based on the graphical representation of the derived data upon all characteristic reference planes, it was apparent that no stratified flow layers were developed throughout the electric heater domain. Therefore, the final design of the electric heater was found to be appropriate for eliminating any risk for thermal stratification development. More specifically, in each specific baffle section, the developed temperature field was merely homogeneous, and no stratified layers were developed. Furthermore, the absolute values of the static temperature of molten salt were gradually increasing along the -z direction. This is normal, since as the working medium flows through the component, the working medium further heats up. However, the increase in the molten salt temperature in subcase 2 was more abrupt, since it was supposed that 80% of the heat duty was delivered in the first 60% of the length of the heater. Furthermore, in both scenarios, the last baffle sections were characterized by the highest absolute static temperatures of the working medium flow inside the domain.

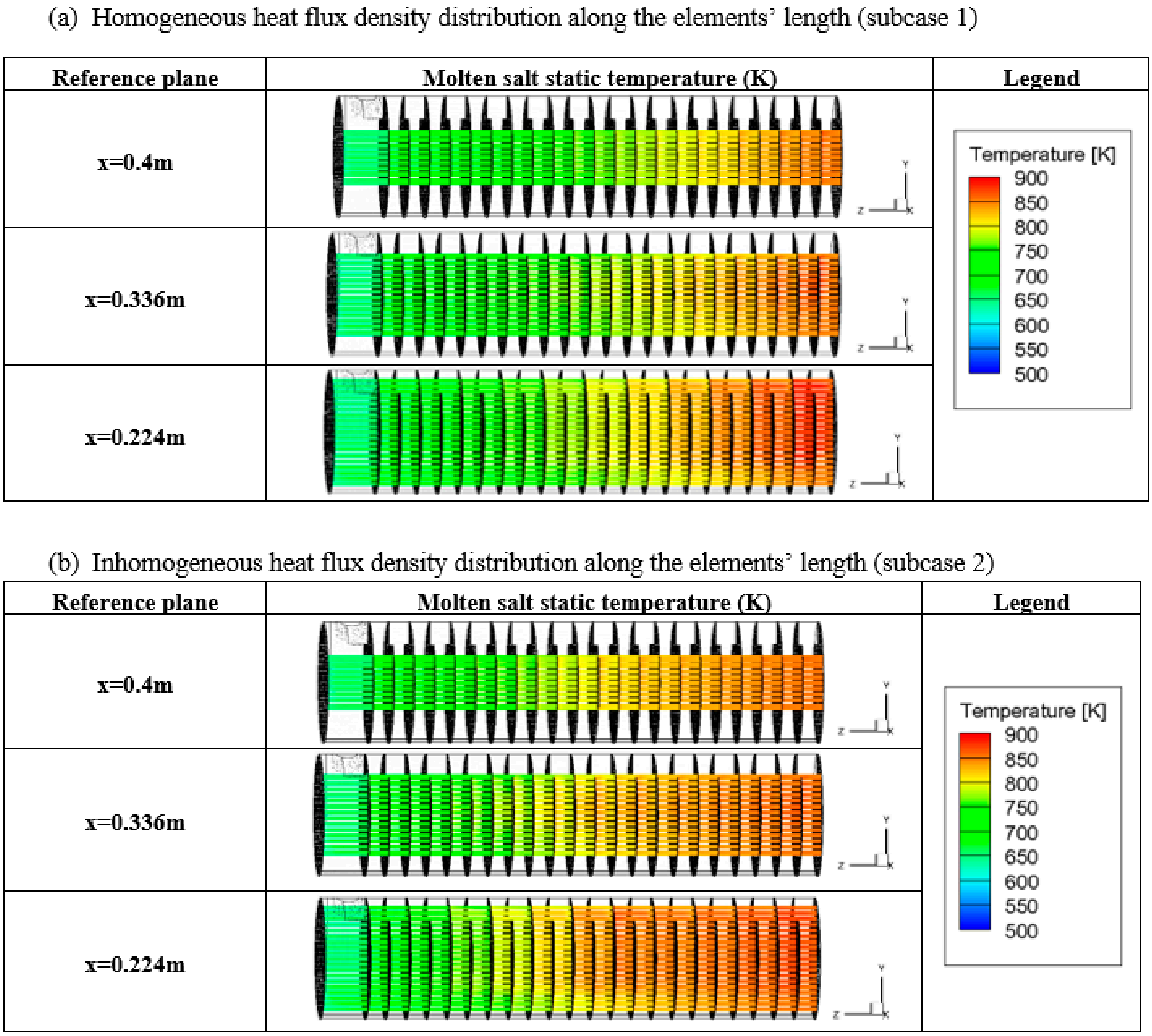


**Figure 9.** Molten-salt static temperature (K) spatial distribution at different characteristic planes (+x).

However, these values are still above the upper acceptable limit of 873.15 K/600 °C, where degradation is likely to evolve. In addition, it can be detected that in both cases some hot spots occurred underneath the longitudinal plate, which were more visible at x = 0.112 m and x = −0.112 m surfaces. This feature was more intense in the case with the inhomogeneous heat flux density spatial distribution (i.e., subcase 2). Apparently, the flow of the working medium underneath the geometric configuration of the longitudinal plate and the high concentration of electric heater elements in this specific zone resulted in the formation of hot spots. In order for this to be avoided, specific adjustment of the element arrangement, heat density of the central elements, or the modification of the total heat duty provided may play a critical role.

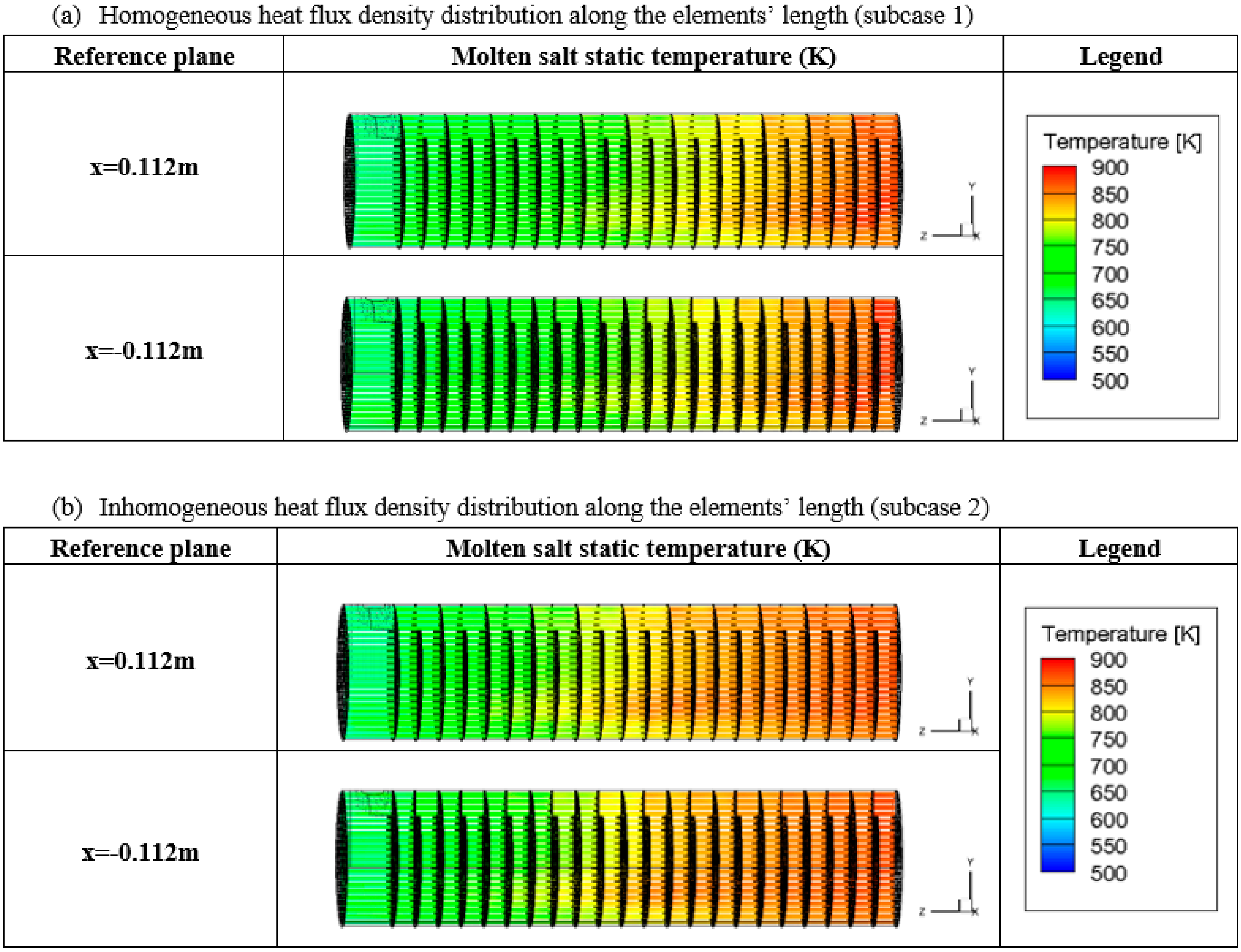


**Figure 10.** Molten-salt static temperature (K) spatial distribution at different characteristic planes close to the centerline (x = 0).

The formation of hot spots underneath the longitudinal plate in both cases is also visible in Figure 12, where the iso-surfaces of 873 K/600 °C are provided. As can be seen in these contours, hot spots were indeed developed in both cases. Furthermore, the final stages of the electric heater presented in both cases the static temperature values of the working medium just equal to or higher than the upper acceptable limit (873 K/600 °C); thus, further decisions on the implemented total heat duty or the loading of the central electric heater elements need to be made. Furthermore, in subcase 2, the formation of a high-temperature zone was also visible downstream of the electric heater middle length, i.e., the transition zone of the heat flux density values. This zone included central areas of the electric heater, thus zones with a high concentration of electric heater elements. Therefore, when the heat duty is delivered unequally, it is possible that certain parts of the electric heater will heat up the working medium flow rather abruptly, thereby forming extensive areas of high temperature and imposing risks for the normal operation of the component. Therefore, homogeneous heat provision along the full length of the elements is preferable.

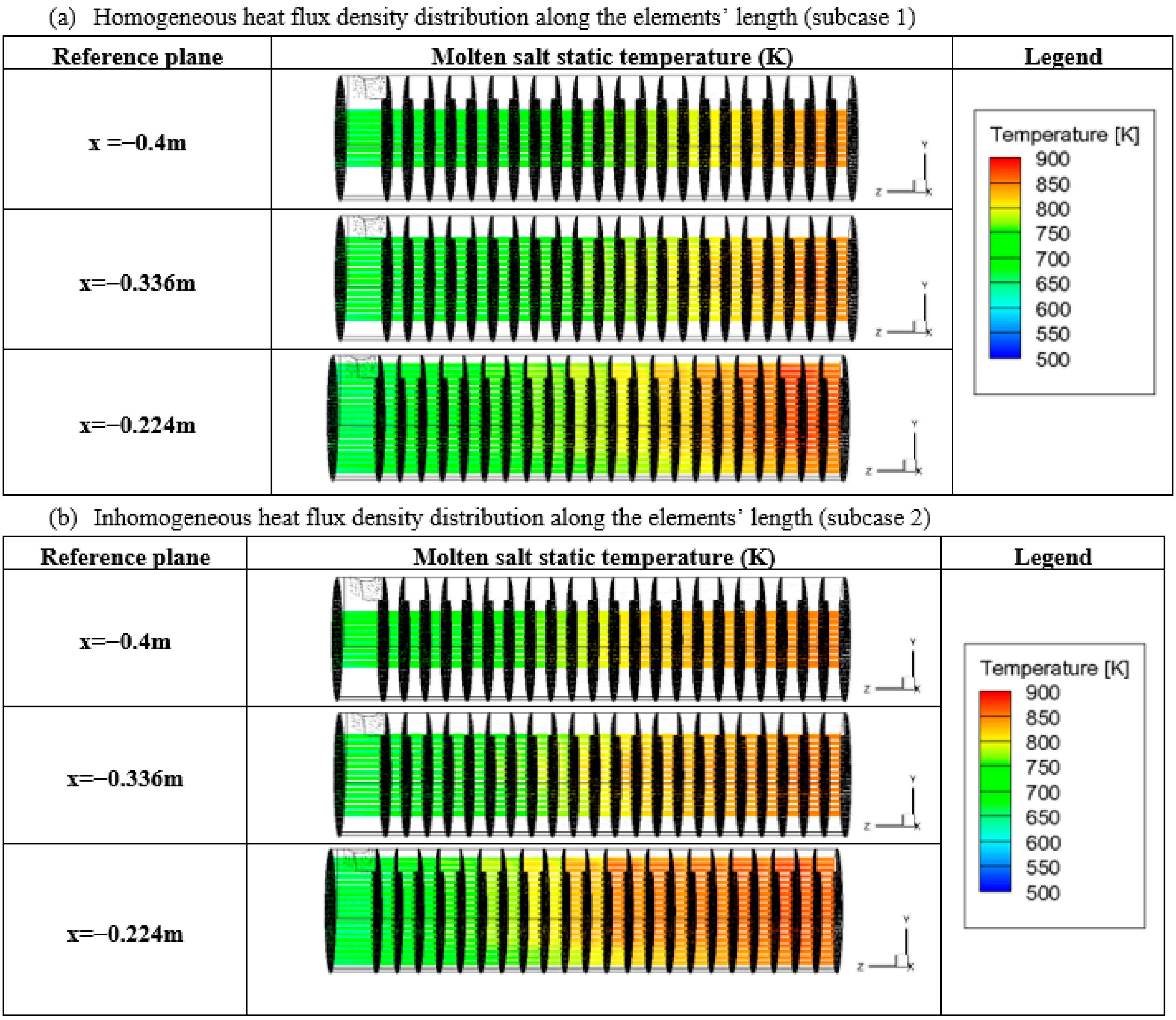


**Figure 11.** Molten-salt static temperature (K) spatial distribution at different characteristic planes (−x).

Overall, even if the formation of very high temperature values was not avoided with the new configuration of the electric heater, thermal stratification was not present. Therefore, this new design minimizes the risks for such operational issues.

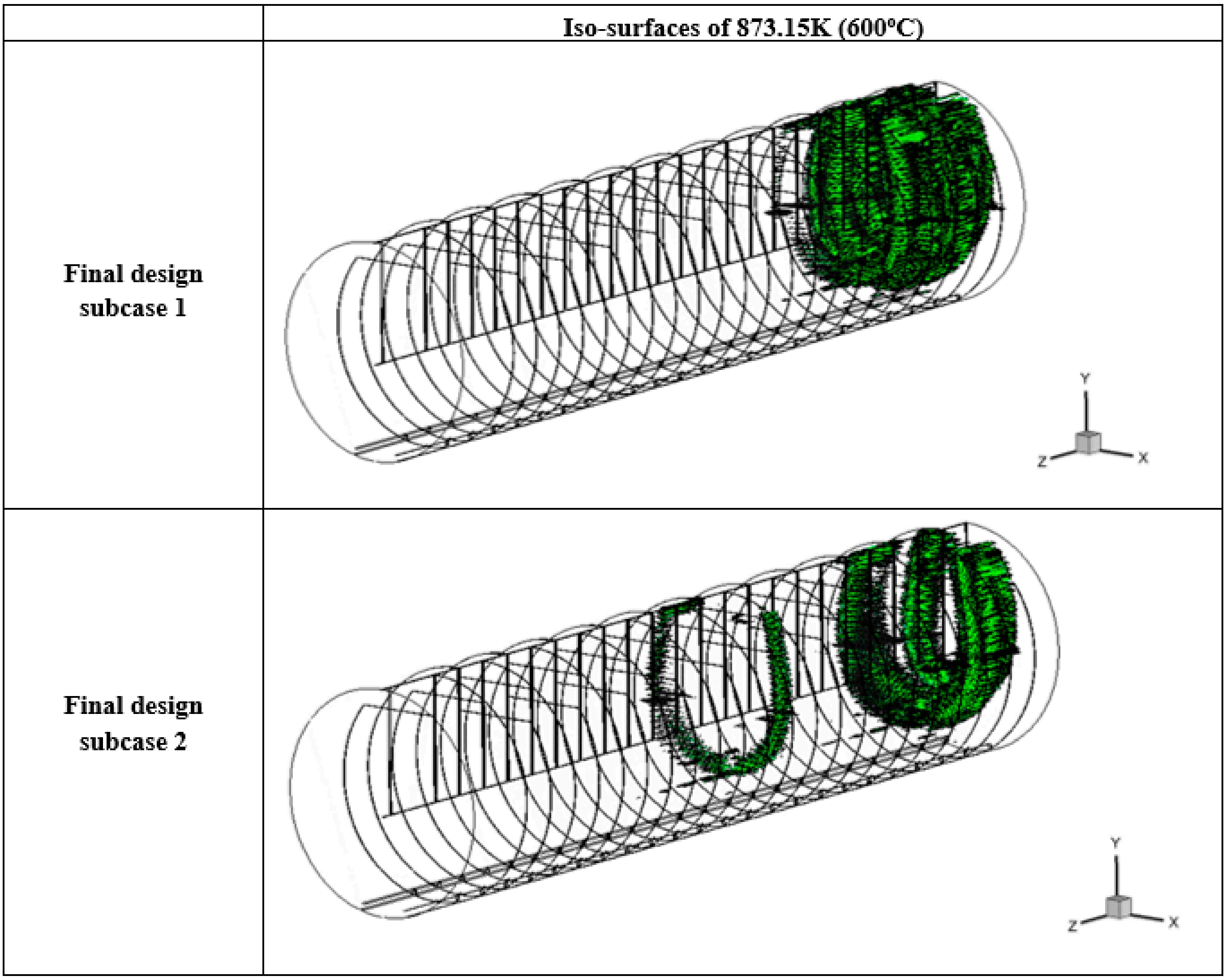


**Figure 12.** Comparison of iso-surfaces (K) between the two subcases of the final electric heater design simulation.

## 4. Conclusions

A significant decrease in greenhouse gas emissions can be achieved via the widespread adoption of grid-level electricity generation from CSP systems. To further enhance the efficiency and expand the application potential of such systems, the combination of s-$CO_2$ Brayton cycles with recirculating molten salt utilized as a heat transfer fluid presents a highly promising configuration for the next-generation CSP plants. Implementation of a robust, efficient molten-salt electric heater is essential for enabling this technology; however, optimized designs that take into account the wide range of particularities pertinent to molten salt flow and heat transfer phenomena are yet to be developed. In this study, we present the findings of CFD simulations, demonstrating that the development of thermal stratification and hot spots are the main challenges impeding the efficient design of electric heaters for next-generation $sCO_2$–molten-salt CSP plants.

The main conclusions drawn from this analysis are summarized below:

- Thermal stratification and the development of hot spots pose significant challenges for the efficient design of electric heaters in next-generation $sCO_2$–molten-salt CSP plants. Proper consideration of the molten salt flow conditions and component geometry (including the dimensioning, spacing, and arrangement of the heating elements and baffles) can mitigate such phenomena at an appreciable level.

- Various electric heater configurations were developed and numerically tested, yielding an optimized, horizontally configured design that enhances turbulence intensity and reduces the stratification risk.
- While complete elimination of hot spots may not be feasible, applying a homogeneous distribution of heat flux density across the electric heater elements offers the most favorable option in terms of temperature spatial distribution and elimination of hot spots.

Notably, the main conclusions drawn here align well with those derived from a previous CFD study [27], emphasizing the significance of optimized geometric features (such as the characteristics of clearances and number of baffles) in mitigating the occurrence of dead zones and hot spots within similar electric heaters.

**Author Contributions:** Conceptualization, P.D., G.I. and N.N.; methodology, P.D., G.I. and N.N.; software, P.D.; writing—original draft preparation, P.D.; writing—review and editing, G.I. and N.N.; visualization, P.D.; supervision, N.N. All authors have read and agreed to the published version of the manuscript.

**Funding:** This project has received funding from the European Union's Horizon 2020 research and innovation programme under grant agreement No 952953.

**Data Availability Statement:** Data available on request due to restrictions.

**Conflicts of Interest:** The authors declare no conflict of interest.

## Abbreviations

| | |
|---|---|
| Computer-Aided Design | CAD |
| Computational Fluid Dynamics | CFD |
| Concentrated Solar Power | CSP |
| Heat Transfer Fluid | HTF |
| Photovoltaic | PV |
| Random Access Memory | RAM |
| Renewable Energy | RE |
| Renewable Energy Sources | RES |
| Thermal Energy Storage | TES |

## References

1. Barberis, S.; Traverso, A.N.; Traverso, A.; Massardo, A.F. High Temperature Storage for CSP Hybrid Gas Turbine: Test Rig Dynamic Analysis and Experimental Validation. In Proceedings of the ASME Turbo Expo 2016: Turbomachinery Technical Conference and Exposition, Seoul, Republic of Korea, 13–17 June 2016; Volume 3. [CrossRef]
2. Magrassi, F.; Rocco, E.; Barberis, S.; Gallo, M.; Del Borghi, A. Hybrid solar power system versus photovoltaic plant: A comparative analysis through a life cycle approach. *Renew. Energy* **2019**, *130*, 290–304. [CrossRef]
3. Pitz-Paal, R. 19—Concentrating Solar Power. In *Future Energy*, 3rd ed.; Letcher, T.M., Ed.; Elsevier: Amsterdam, The Netherlands, 2020; pp. 413–430. [CrossRef]
4. Sivaram, V. *Taming the Sun: Innovations to Harness Solar Energy and Power the Planet*; The MIT Press: Cambridge, MA, USA, 2018.
5. Tzivanidis, C.; Bellos, E.; Antonopoulos, K.A. Energetic and financial investigation of a stand-alone solar-thermal Organic Rankine Cycle power plant. *Energy Convers. Manag.* **2016**, *126*, 421–433. [CrossRef]
6. Wang, K.; He, Y.-L.; Zhu, H.-H. Integration between supercritical $CO_2$ Brayton cycles and molten salt solar power towers: A review and a comprehensive comparison of different cycle layouts. *Appl. Energy* **2017**, *195*, 819–836. [CrossRef]
7. Caccia, M.; Tabandeh-Khorshid, M.; Itskos, G.; Strayer, A.R.; Caldwell, A.S.; Pidaparti, S.; Singnisai, S.; Rohskopf, A.D.; Schroeder, A.M.; Jarrahbashi, D.; et al. Ceramic–metal composites for heat exchangers in concentrated solar power plants. *Nature* **2018**, *562*, 406–409. [CrossRef] [PubMed]
8. Turchi, C.S.; Ma, Z.; Neises, T.W.; Wagner, M.J. Thermodynamic Study of Advanced Supercritical Carbon Dioxide Power Cycles for Concentrating Solar Power Systems. *J. Sol. Energy Eng.* **2013**, *135*, 041007. [CrossRef]
9. Wood, L. 2020 Global Market for Concentrated Solar Power Market Analysis—CSP Could Provide Up to 25% of World Energy Needs by 2050. Globe News Wire. 2020. Available online: https://www.globenewswire.com/news-release/2020/11/06/2121927/28124/en/2020-Global-Market-for-Concentrated-Solar-Power-Market-Analysis-CSP-Could-Provide-Up-to-25-of-World-Energy-Needs-by-2050.html (accessed on 8 March 2022).

10. Márquez, F.P.G.; Karyotakis, A.; Papaelias, M. *Renewable Energies: Business Outlook 2050*; Springer International Publishing: Berlin/Heidelberg, Germany, 2018; Available online: https://books.google.gr/books?id=aaRMDwAAQBAJ (accessed on 11 April 2022).
11. Weinstein, L.A.; Loomis, J.; Bhatia, B.; Bierman, D.M.; Wang, E.N.; Chen, G. Concentrating Solar Power. *Chem. Rev.* **2015**, *115*, 12797–12838. [CrossRef] [PubMed]
12. Denholm, P.; Mehos, M. The Role of Concentrating Solar Power in Integrating Solar and Wind Energy. In Proceedings of the 4th Solar Integration Workshop, Berlin, Germany, 11–13 November 2014; p. 6.
13. Du, E.; Zhang, N.; Kang, C.; Miao, M.; Tian, X. Exploring the flexibility of CSP for wind power integration using interval optimization. In Proceedings of the 2016 IEEE Power and Energy Society General Meeting (PESGM), Boston, MA, USA, 17–21 July 2016; pp. 1–5. [CrossRef]
14. Vignarooban, K.; Xu, X.; Arvay, A.; Hsu, K.; Kannan, A.M. Heat transfer fluids for concentrating solar power systems—A review. *Appl. Energy* **2015**, *146*, 383–396. [CrossRef]
15. Crespi, F.; Toscani, A.; Zani, P.; Sánchez, D.; Manzolini, G. Effect of passing clouds on the dynamic performance of a CSP tower receiver with molten salt heat storage. *Appl. Energy* **2018**, *229*, 224–235. [CrossRef]
16. Delise, T. Technical and economic analysis of a CSP plant presenting a low freezing ternary mixture as storage and transfer fluid. *Appl. Energy* **2020**, *265*, 114676. [CrossRef]
17. Caldwell, A.S.; Itskos, G.; Sandhage, K.H. Air-stable, earth-abundant molten chlorides and corrosion-resistant containment for chemically-robust, high-temperature thermal energy storage for concentrated solar power. *Mater. Today* **2021**, *46*, 9–17. [CrossRef]
18. Gong, Q.; Shi, H.; Chai, Y.; Yu, R.; Weisenburger, A.; Wang, D.; Bonk, A.; Bauer, T.; Ding, W. Molten chloride salt technology for next-generation CSP plants: Compatibility of Fe-based alloys with purified molten $MgCl_2$-KCl-NaCl salt at 700 °C. *Appl. Energy* **2022**, *324*, 119708. [CrossRef]
19. Trevisan, S.; Guédez, R.; Laumert, B. Thermodynamic analysis of an indirect supercritical $CO_2$—Air driven concentrated solar power plant with a packed bed thermal energy storage. In Proceedings of the SOLARPACES 2019: International Conference on Concentrating Solar Power and Chemical Energy Systems, Daegu, Republic of Korea, 1–4 October 2019; p. 130007. [CrossRef]
20. Prieto, C.; Cabeza, L.F. Thermal energy storage with phase change materials in solar power plants. Economic analysis. *J. Energy Storage* **2021**, *43*, 103184. [CrossRef]
21. Yang, Y.; Guo, S.; Liu, D.; Li, R.; Chu, Y. Operation optimization strategy for wind-concentrated solar power hybrid power generation system. *Energy Convers. Manag.* **2018**, *160*, 243–250. [CrossRef]
22. Ferri, R.; Cammi, A.; Mazzei, D. Molten salt mixture properties in RELAP5 code for thermodynamic solar applications. *Int. J. Therm. Sci.* **2008**, *47*, 1676–1687. [CrossRef]
23. Gaggioli, W.; Fabrizi, F.; Tarquini, P.; Rinaldi, L. Experimental Validation of the Innovative Thermal Energy Storage Based on an Integrated System "Storage Tank/Steam Generator". *Energy Procedia* **2015**, *69*, 822–831. [CrossRef]
24. Hu, S.; Finklea, H.; Liu, X. A review on molten sulfate salts induced hot corrosion. *J. Mater. Sci. Technol.* **2021**, *90*, 243–254. [CrossRef]
25. Ma, L.; Zhang, C.; Wu, Y.; Lu, Y. Comparative review of different influence factors on molten salt corrosion characteristics for thermal energy storage. *Sol. Energy Mater. Sol. Cells* **2022**, *235*, 111485. [CrossRef]
26. Bell, S.; Steinberg, T.; Will, G. Corrosion mechanisms in molten salt thermal energy storage for concentrating solar power. *Renew. Sustain. Energy Rev.* **2019**, *114*, 109328. [CrossRef]
27. Mahdi, Z.; Merige, P.S.; Caminos, R.A.C.; Schmitz, P.; Herrmann, U.; Boura, C.T.; Schmitz, M.; Gielen, H.; Gedle, Y.; Dersch, J. Modeling the thermal behavior of solar salt in electrical resistance heaters for the application in PV-CSP hybrid power plants. In Proceedings of the SOLARPACES 2020: 26th International Conference on Concentrating Solar Power and Chemical Energy Systems, Freiburg, Germany, 28 September–2 October 2020; p. 030013. [CrossRef]